



**HAL**  
open science

# Optimal multiple motion encoding in Phase-Contrast MRI

Helge Herthum, Hugo Carrillo, Axel Osses, Sergio Uribe, Ingolf Sack,  
Cristobal Bertoglio

► **To cite this version:**

Helge Herthum, Hugo Carrillo, Axel Osses, Sergio Uribe, Ingolf Sack, et al.. Optimal multiple motion encoding in Phase-Contrast MRI. 2020. hal-02947225v2

**HAL Id: hal-02947225**

**<https://hal.science/hal-02947225v2>**

Preprint submitted on 12 Dec 2020 (v2), last revised 17 Mar 2022 (v4)

**HAL** is a multi-disciplinary open access archive for the deposit and dissemination of scientific research documents, whether they are published or not. The documents may come from teaching and research institutions in France or abroad, or from public or private research centers.

L'archive ouverte pluridisciplinaire **HAL**, est destinée au dépôt et à la diffusion de documents scientifiques de niveau recherche, publiés ou non, émanant des établissements d'enseignement et de recherche français ou étrangers, des laboratoires publics ou privés.

# Optimal multiple motion encoding in Phase-Contrast MRI

Helge Herthum<sup>1,\*</sup>, Hugo Carrillo<sup>2</sup>, Axel Osses<sup>2,3</sup>  
Sergio Uribe<sup>3,4</sup>, Ingolf Sack<sup>1</sup>, Cristóbal Bertoglio<sup>5,\*†</sup>

<sup>1</sup>Department of Radiology, Charité - Universitaetsmedizin Berlin, Berlin, Germany

<sup>2</sup>Center for Mathematical Modeling, Universidad de Chile, Santiago, 8370456, Chile

<sup>3</sup>ANID – Millennium Nucleus in Cardiovascular Magnetic Resonance, Santiago, 7820436, Chile

<sup>4</sup>Biomedical Imaging Center, Pontificia Universidad Catolica de Chile, Santiago, 7820436, Chile

<sup>5</sup>Bernoulli Institute, University of Groningen, Groningen, 9747AG, The Netherlands

December 12, 2020

## Abstract

**Purpose:** To propose an optimal multiple motion encoding method (OMME) for phase-contrast MRI with application to Magnetic Resonance Elastography (MRE) for unwrapping motion images.

**Theory:** OMME is formulated as a least-squares problem for the motion using an arbitrary number of phase-contrast measurements with different motion encoding gradients (MEG). The mathematical properties of OMME are proved in terms of standard deviation and dynamic range of the motion's estimate.

**Methods:** OMME's performance is assessed on MRE data from heparin phantom experiments and from in vivo human brain experiments for the most robust MEG combination obtained by the theory. The unwrapped wave images are further used to reconstruct shear wave speed (SWS) maps and compared to the ones obtained using conventional phase unwrapping methods.

**Results:** OMME allowed to successfully combine three and four MRE wave images with different dynamic ranges in the phantom and volunteer data, respectively. This leads to improved motion-to-noise ratio (MNR) in the measured waves and therefore to SWS maps with greater resolution of details than obtained with conventional unwrapping methods.

**Conclusion:** The proposed OMME method allows for effective increase in the dynamic range of phase-contrast images with respect to the number of MEGs while maintaining the MNR of the image with the lowest dynamic range. The method may be especially suitable for applications where high resolution MRE images with high MNR are needed.

---

\*Equally contributing authors

†Corresponding author: [c.a.bertogliorug.nl](mailto:c.a.bertogliorug.nl)

# 1 Introduction

Phase-contrast Magnetic Resonance Imaging (PC-MRI) is a well-established method for measuring flow velocities [24] or tissue displacements due to harmonic excitation as used in Magnetic Resonance Elastography (MRE) [9, 15, 14, 23, 11, 17, 8, 5, 10].

Motion is encoded in the phase of the complex transverse magnetization proportional to the encoding efficiency of the motion encoding gradient (MEG). However, the phase can only be measured in the half-open interval  $[-\pi, \pi)$  and phase wraps (abrupt jumps of  $\pm 2\pi$ ) occur if the encoded phase exceeds those limits. Consequently, for a given encoding efficiency, there is a fixed amplitude range or *dynamic range*, where motion can be acquired without phase wraps. If the encoding efficiency is too large and the true motion amplitude exceeds the dynamic range, phase wraps occur. Unfortunately, selecting a large dynamic range leads to poor quality images since – for a given signal-to-noise-ratio (SNR) in the magnitude image – the “motion-to-noise-ratio” (MNR) is proportional to the dynamic range.

There are usually two approaches to remove the wraps.

First, unwrapping algorithms have been developed by assuming that the motion field is smooth in space, see e.g. [2, 13] and references therein. Nevertheless, they cannot recover the true underlying motion and often fail when the aliased regions are highly heterogeneous, subject to noise or include nested wraps. In such cases, the unwrapped phase appears to be distorted and obstructs further data processing steps. For instance, the simple  $2\pi$ -unwrapping Flynn [7] algorithm is inherently two-dimensional and fails to unwrap noisy complex wraps when no well-defined enclosed region exists. The true motion cannot be recovered because arbitrary  $2\pi$ -offsets are added. Gradient based algorithms [18] only yield the derivative of the phase and amplify noise. Laplacian based unwrapping algorithms [20] remove the constant and linear terms from the data and induce spatial smoothing, altering the resulting phase where important details may be lost.

Second, voxelwise motion reconstructions using dual-encoding strategies have been proposed in PC-MRI which are based on unwrapping low dynamic-range data by exploiting high-dynamic range data [4]. In other words, measurements with a reduced dynamic range (hence, improved MNR) are unwrapped using a measurement with a larger dynamic range. Those methods are performed at each voxel independently and therefore they do not assume or enforce smoothness of the motion-encoded phase field [12, 19, 28]. This allows the reconstruction of the correct motion images, however, at the cost of additional measurements. To the best of the authors’ knowledge, there is neither a reported analysis of MNR in dual encoding nor an extension to multiple motion encoding.

Hence, the aim of this work is threefold.

Firstly, we mathematically and numerically analyze dual motion-encoding strategies to answer the question: Which combination of MEGs provides the smallest noise in the motion image for a given dynamic range and noise level in the phase images?

Secondly, we will use our previously introduced mathematical framework of *optimal dual-encoding* [4] for an extension to multiple motion encoding in MRE, henceforth termed Optimal Multiple Motion Encoding (OMME).

And thirdly, it will be shown that OMME can successfully provide wrap-free low dynamic range MRE phase images for phantom and in vivo brain experiments which are closest to the true underlying motion in the range of MNR of the smallest dynamic range. Reconstructed wrap-free phase images are used as input for the MRE reconstruction that permits recovering more details in SWS maps than commonly phase-unwrapped input images.

## 2 Theory

This section presents the OMME method and its mathematical analysis. Although OMME can be applied to any PC-MRI modality, for the sake of clarity the method is explained using the example of MRE.

### 2.1 Single motion-encoding in PC-MRI

For a given MEG  $G$ , the model of measured phase can be written in the form

$$\varphi_G(u) = \varphi_0 + \delta_G + u \frac{\pi}{d_G} + \varepsilon\pi \quad (1)$$

with the following notation:

- $\varphi_0$  is the reference phase due to the static field inhomogeneities,
- $\delta_G$  is a MEG-dependent phase induced e.g by eddy currents and Maxwell effects,
- $d_G$  is the “dynamic range”, i.e. the inverse of the encoding efficiency depending on the MEG’s amplitude, duration, shape and relative phase of the mechanical wave,
- $u$  denotes the tissue harmonic displacement in the direction of the MEG,
- $\varepsilon \sim \mathcal{N}(0, \sigma_\varphi^2)$  represents the measurement noise in the phase. The value of  $\sigma_\varphi^2$  depends on the SNR of the magnitude measurements.

We will also denote  $u_{true}$  the ground truth displacement.

Notice that we have neglected the contribution of the phase encoded by the imaging gradients. This assumption is justified since the imaging gradients are usually velocity compensated and only higher order terms contribute.

In the case of MRE, the motion-independent phase  $\varphi_G(0) = \varphi_0 + \delta_G$  can be removed by:

1. Either measuring  $\varphi_G(u)$  using a MEG at sufficient equidistant timepoints and separate the harmonic oscillation by the temporal Fourier transform,
2. Or measuring and subtracting the offset phase directly by repeating the experiment without external vibrations for one time step.

The latter approach will be used in the remainder of this work.

Assuming now that  $\varphi_G(u)$  and  $\varphi_G(0)$  is measured (including noise),  $u$  can be estimated as:

$$u = (\varphi_G(u) - \varphi_G(0)) \frac{d_G}{\pi} - (\varepsilon_u - \varepsilon_0) d_G \quad (2)$$

with  $\varepsilon_u$  and  $\varepsilon_0$  independent realizations of  $\varepsilon$  for the two phase measurements. Consequently,  $u \sim \mathcal{N}(\bar{u}, 2d_G^2\sigma_\varphi^2)$  since at least two phase measurements are needed due to the unknowns  $u$  and  $\varphi_G(0)$ . Consequently,  $d_G$  should be chosen as small as possible.

However, phase can be measured only within the interval  $[-\pi, \pi)$ . Hence, if  $d_G < |u_{true}|$  (if  $\sigma_\varphi = 0$ ) then the measured displacement  $u$  wraps by a multiple of  $2d_G$ . Naturally, aliasing can occur even if  $d_G > |u_{true}|$  in the presence of noise  $\varepsilon \neq 0$ .

For a given dynamic range, a natural approach to reduce the variance of  $u$  is to average more measurements. If  $n$  is the number of measurements made of  $\varphi_G$  (always with the same  $d_G$ ) and  $n_0$  the number of measurements of  $\varphi_G(0)$ , then

$$u \sim \mathcal{N}(\bar{u}, d_G^2 \sigma_\varphi^2 (n^{-1} + n_0^{-1})) = \begin{cases} \mathcal{N}(\bar{u}, \left(\frac{d_G}{\sqrt{n}}\right)^2 \sigma_\varphi^2), & n \ll n_0 \\ \mathcal{N}(\bar{u}, 2 \left(\frac{d_G}{\sqrt{n}}\right)^2 \sigma_\varphi^2), & n = n_0 \end{cases} \quad (3)$$

From this relation it is clear that decreasing  $d_G$  is more effective than increasing the number of measurements  $n$ , since the standard deviation of  $u$  decreases linearly with respect to  $d_G/\sqrt{n}$ .

## 2.2 Classical dual motion encoding revisited

The basic idea of multiple motion encoding approaches is to include additional measurements with a reduced value of  $d_G$  (e.g., larger MEGs) while keeping the dynamic range of the motion-sensitive phase image large. In this section we will treat the case of dual encoding, i.e. for two different values  $d_1, d_2$  for  $d_G$ .

We assume now that we measure phases with two different MEGs amplitudes  $G_1 < G_2 = G_1/\beta$ , with  $0 < \beta < 1$ , with dynamic ranges  $d_1$  and  $d_2$ , respectively. This results in four measured phases  $\varphi_1 = \varphi_1(u), \varphi_1(0), \varphi_2 = \varphi_2(u), \varphi_2(0)$ . We assume that these values already include the additive noise with zero mean and variance  $\pi^2 \sigma_\varphi^2$  as in Equation (1).

From the four phase measurements, four motion images can then be estimated:

$$u_1 = \frac{\varphi_1 - \varphi_1(0)}{\pi} d_1, \quad u_2 = \frac{\varphi_2 - \varphi_2(0)}{\pi} d_2$$

$$u_{ps} = \frac{\varphi_1 + \varphi_2 - \varphi_1(0) - \varphi_2(0)}{\pi} d_{ps}, \quad u_{pc} = \frac{\varphi_2 - \varphi_1 + \varphi_1(0) - \varphi_2(0)}{\pi} d_{pc}$$

with  $d_{ps} = (d_1^{-1} + d_2^{-1})^{-1}$ ,  $d_{pc} = (d_2^{-1} - d_1^{-1})^{-1}$ . Notice that

$$d_{pc} = d_1 \frac{\beta}{1 - \beta} \geq d_1 > d_2 = \beta d_1 > d_{ps} = d_1 \frac{\beta}{1 + \beta}.$$

and thus we call  $d_{pc} = d_{eff}$  as the *effective dynamic range* of the dual encoding method.

Defining  $\alpha = \sqrt{2} \sigma_\varphi d_1$ , the variances of the different motion estimators satisfy:

$$\text{Var}(u_1) = 2\sigma_\varphi^2 d_1^2 = \alpha^2, \quad \text{Var}(u_2) = 2\sigma_\varphi^2 d_2^2 = \alpha^2 \beta^2$$

$$\text{Var}(u_{pc}) = 4\sigma_\varphi^2 d_{pc}^2 = \alpha^2 \frac{2\beta^2}{(1 - \beta)^2} = \alpha^2 \frac{\beta^2}{\left(\frac{1 - \beta}{\sqrt{2}}\right)^2}, \quad \text{Var}(u_{ps}) = 4\sigma_\varphi^2 d_{ps}^2 = \alpha^2 \frac{2\beta^2}{(1 + \beta)^2} = \alpha^2 \frac{\beta^2}{\left(\frac{1 + \beta}{\sqrt{2}}\right)^2},$$

and therefore

$$\text{Var}(u_{pc}) > \text{Var}(u_1) > \text{Var}(u_2) > \text{Var}(u_{ps}).$$

Dual encoding reconstructions aim to unwrap a motion reconstructed with low dynamic range using a motion reconstructed with a high dynamic range as follows [12]:

$$u_{uw} = u_{low} + 2d_{low} N.I. \left( \frac{u_{high} - u_{low}}{2d_{low}} \right) \quad (4)$$

with  $N.I.$  the nearest integer operator. This leads to  $\text{Var}(u_{uw}) = \text{Var}(u_{low})$  when the unwrapping is successful. This method will be denoted in as *standard dual encoding*. To pick up  $u_{low}$  and  $u_{high}$  we apply the following reasoning. Firstly, we pick  $u_{low} = u_2$  since it possess a higher dynamic range than  $u_{ps}$  (e.g.  $d_{pc} = 3/2d_{ps}$  for  $\beta = 1/2$ ) only with a slightly higher variance (e.g.  $\text{Var}(u_2)/\text{Var}(u_{ps}) = 1.125$  for  $\beta = 1/2$ ). Secondly, we pick

$$u_{high} = \begin{cases} u_1 & \beta \in \{1/2, 1\} \\ u_{pc} & \text{elsewise} \end{cases}$$

since  $u_{pc}$  has the desired effective range  $d_{eff} \geq d_1$ , but for  $\beta = 1/2$  it holds  $d_1 = d_{eff}$  and  $\text{Var}(u_1) < \text{Var}(u_{pc})$ , and for  $\beta = 1$   $u_{pc}$  is not defined and  $d_1 = d_{eff}$ .

### 2.3 The optimal dual motion encoding method [4] revisited

In [4], a new method for unwrapping two motion-encoded images was introduced, *Optimal dual venc* (ODV)- a method originally proposed for flow MRI. In this paragraph we will briefly recall the method, and show some new theoretical results.

The method is based on the formulation of the phase contrast problem as the minimization of cost functional. For the single motion encoding case, the cost functional has the form:

$$J_i(u) = 1 - \cos\left(\varphi_i - \varphi_i(0) - \frac{\pi u}{d_i}\right) = 1 - \cos\left(\frac{\pi}{d_i}(u_i - u)\right)$$

which comes from a least squares approximation for the angle by measuring the components of a vector and where  $\varphi_i$  and  $\varphi_G(0)$  where defined in the previous section.

It is easy to see that the period of  $J_i(u)$  is  $2d_i$ , and therefore local minimum among with smallest value (in absolute terms)  $u_i + 2k_id_i, k_i \in \mathbb{Z}$  corresponds to the the single encoding phase-contrast motion.

For the dual encoding case, the problem shifts from finding the local minima of  $J(u)$  to find the global minima of

$$J_{dual}(u) = J_1(u) + J_2(u) = 2 - \cos\left(\frac{\pi}{d_1}(u_1 - u)\right) - \cos\left(\frac{\pi}{d_2}(u_2 - u)\right).$$

It was proven in [4] that  $u_{true}$  is a global minimum of  $J_{dual}$ . Moreover, as a new result,  $J_{dual}$  has periodicity  $2d_{eff}$  when  $\beta = a/b$ ,  $a < b \in \mathbb{N}$ , see Appendix A for the proof.

In the optimal dual encoding method, the unwrapped motion corresponds to the global minimum with smallest magnitude, which we will denote  $u_*$ . Therefore, due to the  $2d_{eff}$ -periodicity, aliasing will occur when  $d_{eff} \leq |u_{true}|$ . Notice that in opposite than the standard dual encoding for  $\beta \neq 1/2$  we do not need  $u_{pc}$  for unwrapping: both  $u_1$  and  $u_2$  can be aliased, still resulting in an unwrapped  $u_*$ .

In [4], no theoretical noise analysis was performed, which will be shown here. First, we need an expression  $u_*$ , which can be obtained from the fact that the global minimum is also a local minimum, i.e.  $J'_{dual}(u_*) = 0$ . Indeed

$$\begin{aligned} J'_{dual}(u_*) &= -\frac{\pi}{d_1} \sin\left(\frac{\pi}{d_1}(u_1 - u_*)\right) - \frac{\pi}{d_2} \sin\left(\frac{\pi}{d_2}(u_2 - u_*)\right) \\ &= -\frac{\pi}{d_1} \sin\left(\frac{\pi}{d_1}(u_1 + 2k_1d_1 - u_*)\right) - \frac{\pi}{d_2} \sin\left(\frac{\pi}{d_2}(u_2 + 2k_2d_2 - u_*)\right) \end{aligned}$$

for all  $k_1, k_2 \in \mathbb{Z}$ . Notice that  $u_* \approx u_1 + 2k_1d_1 \approx u_2 + 2k_2d_2$  for some fixed  $k_1, k_2$  in case of small measurement noise in the phase (and equal if no noise is present). Hence, we can approximate the sin-terms by its arguments leading to:

$$u_* \approx (d_1^{-2} + d_2^{-2})^{-1} (u_1d_1^{-2} + u_2d_2^{-2} + 2(k_1d_1^{-1} + k_2d_2^{-1})). \quad (5)$$

Since assume all that measurements are statistically independent (and therefore  $u_1$  and  $u_2$ ), the variance of  $u_*$  has the form

$$\text{Var}(u_*) = (d_1^{-2} + d_2^{-2})^{-2} (\text{Var}(u_1)d_1^{-4} + \text{Var}(u_2)d_2^{-4}) \quad (6)$$

$$= (d_1^{-2} + d_2^{-2})^{-2} (\alpha^2d_1^{-4} + \alpha^2\beta^2d_2^{-4}) = \frac{\text{Var}(u_2)}{1 + \beta^2} < \text{Var}(u_2). \quad (7)$$

Thus, an improved estimate in terms of variance is obtained.

Figure 1 presents the previous findings in a graphical way. There, we show the standard deviations of the estimators (i.e. the square root of the variances) versus the effective dynamic ranges for various values of  $\beta$ . The plots are constructed as follows:

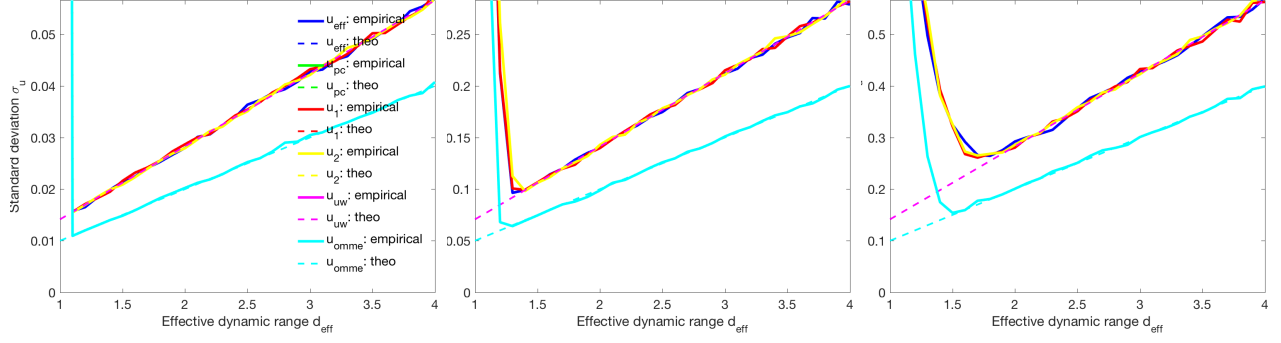
- For a fixed value of  $d_{eff}$  and  $\beta$ ,  $d_1$  and  $d_2$  are computed and 5000 realizations of the measurements for all four phases are generated using a value for  $\sigma_\varphi$ . Here, the ground truth values are  $\bar{u} = 1$  and  $\varphi_1(0) = \phi_0$  and  $\varphi_2(0) = 2\phi_0$ , with  $\phi_0 = 0.9\pi$ .
- Then  $u_1, u_2, u_{uv}, u_*$  are computed. Also  $u_{eff}$  being the single motion phase contrast estimate with  $d_G = d_{eff}$  is computed for comparison.
- The standard deviation of such estimates considering the 5000 realizations is computed.
- The curves are drawn by repeating this procedure in the interval  $d_{eff} \in [1, \dots, 4]$ .
- Four values of  $\beta \in \{1, 1/2, 2/3, 3/4\}$  are used. The value  $\beta = 1$  means that two set of measurements are obtained with the same dynamic range. This serves for better assessing the gains of dual encoding approaches.

Note that the peaks in the empirical curves come from aliasing for the corresponding dynamic range; the larger  $\sigma_\varphi$  the larger the interval where aliasing may occur.

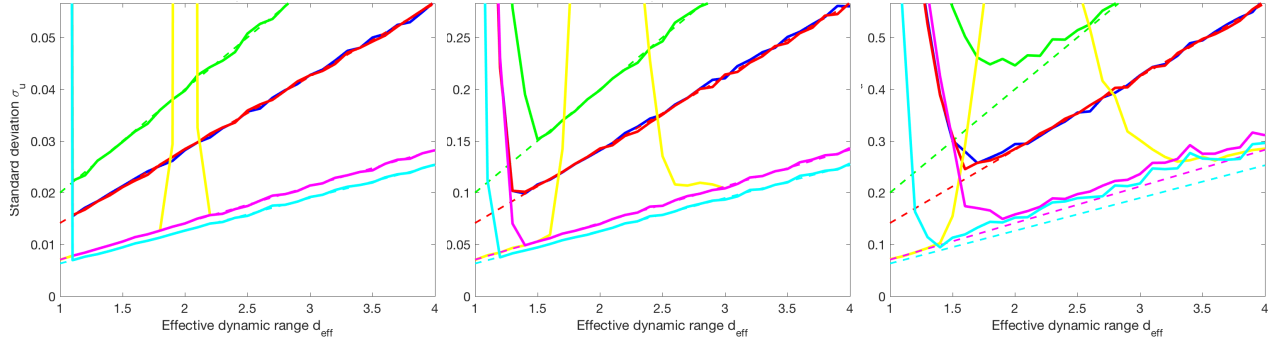
The quality of the results depends on both values of  $\beta$  and  $\sigma_\varphi$ . For small values of  $\sigma_\varphi$ , the empirical and theoretical standard deviations match, but the empirical deviates from the theoretical one when  $d_{eff} \rightarrow |u_{true}|$ , as expected, due to the aliasing. In this low noise scenario, the maximum gain with respect to the case of repeating the same measurements (i.e.  $\beta = 1$ ) is when  $\beta = 3/4$  since for a fixed  $d_{eff}$ ,  $d_1 = d_{eff}/3$  and  $d_2 = d_{eff}/4$ .

However, the reconstruction with  $\beta = 3/4$  becomes unstable when increasing  $\sigma_\varphi$ . The most robust variant with respect to noise for both standard and optimal methods appears to be  $\beta = 1/2$ , where  $d_1 = d_{eff}$  and  $d_2 = d_{eff}/2$ . In case of the optimal method, this can be explained by the fact that the local minima of both  $J_1$  and  $J_2$  cost functionals have maximal distance. For  $\beta = 3/4$ , this distance is much smaller, see details in [4].

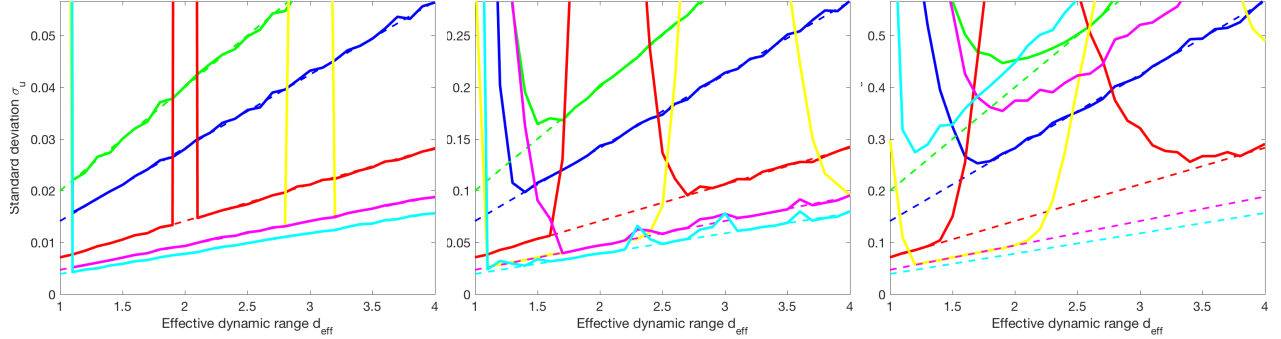
In particular for  $\beta = 1/2$ , between both methods, the optimal dual encoding appears to be more robust with respect to noise, especially when  $d_{eff} \rightarrow |u_{true}|$ , and slightly better than the standard dual encoding approach when  $d_{eff} > |u_{true}|$  due to (6). The possible explanation is



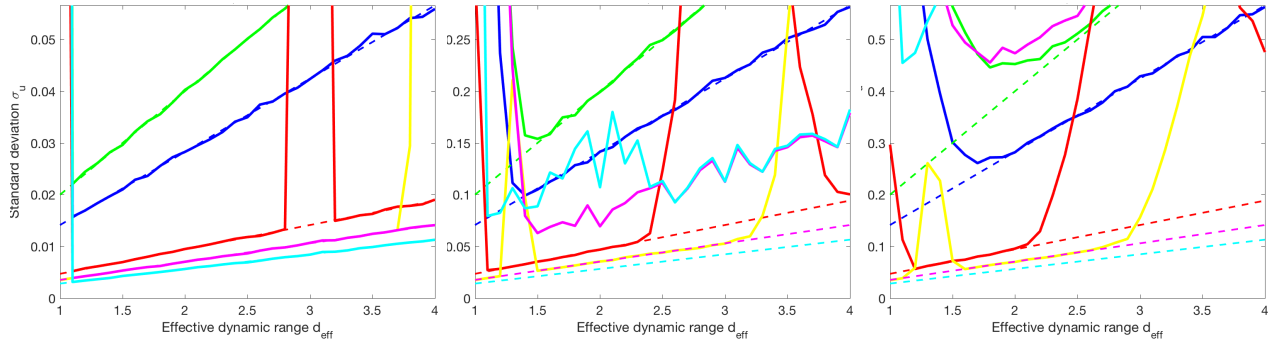
(a)  $\beta = 1$ . The curve for  $u_{pc}$  is not shown since it is not defined. All curves lie on each other except in the optimal method. The region of aliasing becomes larger when increasing  $\sigma_\varphi$ .



(b)  $\beta = 0.5$ . Aliasing occurs for  $u_2$  at  $d_{eff} = 2$ , as expected. All other cases have aliasing limit at  $d_{eff} = 1$ .



(c)  $\beta = 2/3$ . Aliasing occurs for  $u_1$  at  $d_{eff} = 2$  and for  $u_2$  at  $d_{eff} = 3$ , as expected.



(d)  $\beta = 3/4$ . Aliasing occurs for  $u_1$  at  $d_{eff} = 3$  and for  $u_2$  at  $d_{eff} = 4$ , as expected. For this value of  $\beta$ , results become very sensitive to noise.

Figure 1: Single v/s dual motion encoding in one voxel. Left column:  $\sigma_\varphi = 0.01$ . Middle column:  $\sigma_\varphi = 0.05$ . Right column:  $\sigma_\varphi = 0.1$ . The continuous lines represent the empirical variances (i.e. the one computed from the numerical experiments) and the dashed lines the theoretical ones derived before.



that unwrapping and noise compensation are done simultaneously, and therefore, a more robust unwrapping method results.

Henceforth,  $\beta = 1/2$  is used. This choice makes the formulation of a multiple encoding reconstruction easy to implement and analyze. Moreover, it has the practical advantage that at least one image with the desired  $d_{eff}$  is acquired, hence allowing to use standard scan protocols which will be just complemented by the new measurements.

## 2.4 Optimal multiple motion encoding (OMME)

The optimal dual encoding formulation allows a straightforward extension to multiple MEGs, i.e.

$$J_N(u) = \sum_{j=1}^N \left( 1 - \cos \left( \frac{\pi}{d_j} (u_j - u) \right) \right)$$

The multiple motion encoding reconstruction  $u_*$  is then the global minimum of smallest magnitude within  $[-d_{eff}, d_{eff}]$ , with  $d_{eff}$  the dynamic range of OMME. From the proof in Appendix A,  $J_N$  has periodicity equal to the least common multiplier of  $2d_1 = \dots = 2d_N$  when  $d_j = d_1(a/b)^{j-1}$ ,  $a < b \in \mathbb{N}$ , being then  $d_{eff} = a^{N-1}d_1$  half of that periodicity.

Analogously to the dual encoding case, the optimum can be found to approximately be

$$u_* \approx \left( \sum_{j=1}^N d_j^{-2} \right)^{-1} \left( \sum_{j=1}^N u_j d_j^{-2} + 2k_j d_j^{-1} \right), \quad k_j \in \mathbb{Z}, \quad j = 1, \dots, N$$

with variance

$$\begin{aligned} \text{Var}(u_*) &= \left( \sum_{j=1}^N d_j^{-2} \right)^{-2} \sum_{j=1}^N \text{Var}(u_j) d_j^{-4} = 2\sigma_\varphi^2 \left( \sum_{j=1}^N d_j^{-2} \right)^{-2} \sum_{j=1}^N d_j^{-2} \\ &= 2\sigma_\varphi^2 \left( \sum_{j=1}^N d_j^{-2} \right)^{-1} = \text{Var}(u_N) \left( \sum_{j=1}^N \left( \frac{d_N}{d_j} \right)^2 \right)^{-1} < \text{Var}(u_N) \end{aligned}$$

If we consider the case  $d_N = d_j \beta^{N-j}$  for  $j = 1, \dots, N$ , we obtain:

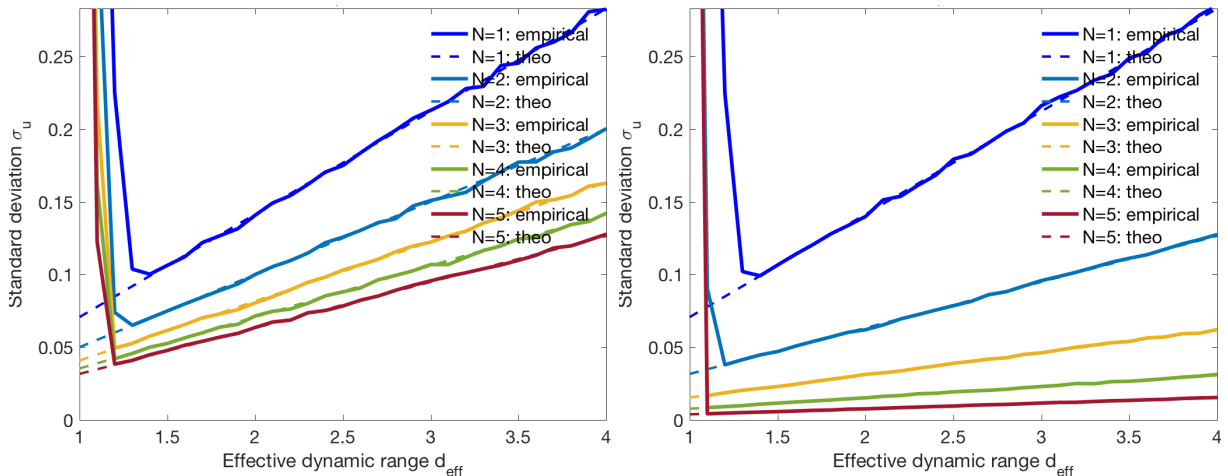
$$\text{Var}(u_*) = \text{Var}(u_N) \beta^{-2N} \left( \sum_{j=1}^N \beta^{-2j} \right)^{-1} = \text{Var}(u_N) \frac{1 - \beta^2}{1 - \beta^{2N}} = \text{Var}(u_1) \beta^{2(N-1)} \frac{1 - \beta^2}{1 - \beta^{2N}}.$$

Note the exponential reduction of the standard deviation with respect to the number of measurements, instead of the linear reduction obtained by averaging equal dynamic range data (i.e.  $\beta = 1$ ).

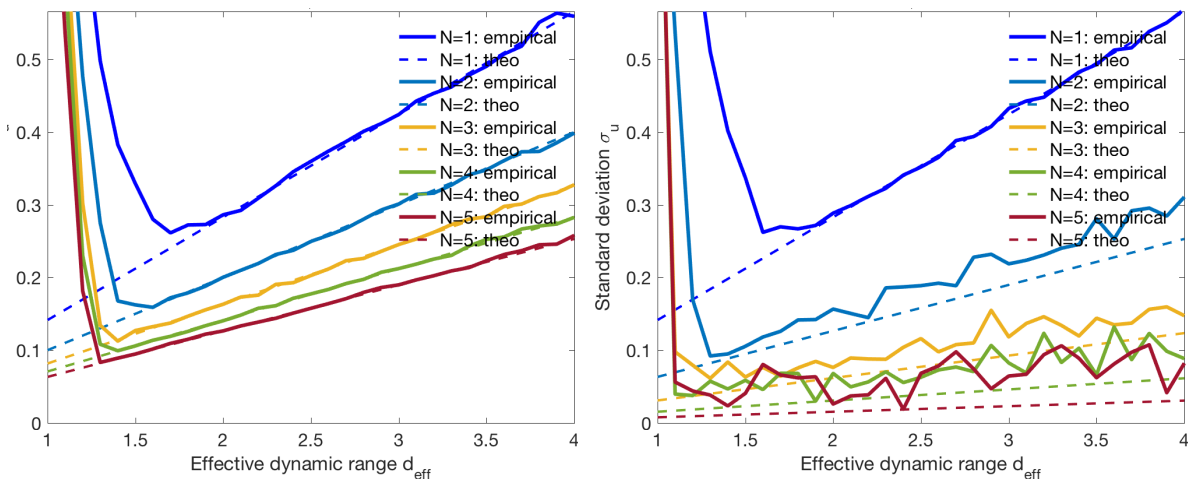
Figure 2 shows the results for the standard deviation versus  $d_{eff}$  for the case of  $\beta = \{1/2, 1\}$  and  $N = 1, \dots, 5$ .

For large noise, i.e.  $\sigma_\varphi = 0.1$ , the empirical standard deviations deviate from the theoretical ones, most likely due to failed unwrapping of noisy data. This is a relevant aspect which implies in practice that noise limits escalation of multiple encoding to an arbitrary number of MEGs. Accordingly, if noise becomes stronger, simple averaging will become the most robust alternative for noise reduction in the motion image.

The theoretical calculations are confirmed and in the case  $\sigma_\varphi = 0.05$  the large superiority of the multiple encoding approach (right,  $\beta = 0.5$ ) compared to averaging (left,  $\beta = 1$ ) in terms of noise reduction can be observed.



(a)  $\sigma_\varphi = 0.05$ . Left:  $\beta = 1$ . Right:  $\beta = 1/2$ .



(b)  $\sigma_\varphi = 0.1$ . Left:  $\beta = 1$ . Right:  $\beta = 1/2$ .

Figure 2: Multiple motion encoding reconstruction. The continuous lines represent the empirical variances (i.e. the one computed from the numerical experiments) and the dashed lines the theoretical ones.

### 3 Methods

#### 3.1 Phantom experiments

Phantom tests were performed using heparin-sodium gel (180 000 IU per 100 g, Ratiopharm, Ulm, Germany) in a 2 L cubic container to experimentally confirm our theory of OMME. The gel mainly consists of Carbomer 980 (polyacrylic acid), trometamol (TRIS), glycerol hydroxystearate,

propylene glycol, and isopropanol with the eponymous active agent only accounting for less than 1% of the gel volume. All experiments were performed in a 3-Tesla MRI scanner (Siemens Magnetom Lumina, Erlangen, Germany).

Air cavities in the phantom material were exploited for the assessment of the fidelity of detail resolution in the MRE maps.

External harmonic vibrations at 30.03 Hz were induced by a pressurized air driver operating at 150 mBar as described elsewhere [21]. The driver was connected to a plate vertically immersed in the gel to reduce vibrations of the casing and to provide plane wave propagation in mainly one direction. The setup is shown in Figure 3. The vibrations were induced 2 s before the start of data acquisition to ensure that a steady state of time-harmonic oscillations was established.

One wavefield component along the top-bottom direction was acquired by using a single-shot, spin-echo echo-planar imaging sequence with flow-compensated MEG. Eight phase offsets over a full vibration period were recorded in 10 coronal slices with  $130 \times 160 \text{ mm}^2$  field of view and  $1.27 \times 1.27 \times 0.9 \text{ mm}^3$  voxel size. Further imaging parameters were: echo time = 165 ms; repetition time = 2500 ms; flip angle  $90^\circ$ ; MEG frequency of 29.45 Hz and MEG amplitude of  $\{4, 8, 16, 32\}$  mT/m respectively. The experiment was repeated without external vibrations to measure  $\varphi_G(0)$  (see Section 2). Therefore,  $\varphi_G(0)$  contains phase offsets from MEG induced eddy currents and involuntary patient motion. One image per encoding direction needs to be acquired. Encoded phase of harmonic motion from imaging gradients can be neglected due to their low encoding efficiency.

### 3.2 Volunteers

In vivo MRE was performed in two male 29-years-old healthy volunteers. The study was approved by the ethics committee of Charite Universitaetsmedizin Berlin in accordance with the Ethical Principles for Medical Research Involving Human Subjects of the World Medical Association Declaration of Helsinki. The participant gave written informed consent.

For each volunteer a different measurement protocol was used to demonstrate robustness of OMME and to explore different features of the method. For volunteer 1 external harmonic vibrations at 25 Hz were introduced by two pressurized air drivers placed under the volunteers head and operated in alternate fashion similar to [21]. Three components of the wavefield in orthogonal directions were acquired without flow-compensated MEGs. Eight phase offsets over a full vibration period were recorded at 11 transversal slices (50% slice gap) with a field-of-view of  $200 \times 200 \text{ mm}^2$  and  $2 \times 2 \times 2 \text{ mm}^3$  voxel size. Further imaging parameters were: echo time = 81 ms; repetition time = 1750 ms; flip angle  $80^\circ$ ; MEG frequency of 27.75 Hz and MEG amplitude of  $\{4, 8, 16, 32\}$  mT/m respectively.

For volunteer 2 external harmonic vibrations at 30.03 Hz were used and three components of the wavefield in orthogonal directions were acquired with flow-compensated MEGs. Eight phase offsets over a full vibration period were recorded at 18 transversal slices (no slice gap) with a field-of-view of  $202 \times 202 \text{ mm}^2$  and  $1.6 \times 1.6 \times 2 \text{ mm}^3$  voxel size. Further imaging parameters were: echo time = 67 ms; repetition time = 2110 ms; flip angle  $81^\circ$ ; MEG frequency of 37.76 Hz and MEG amplitude of  $\{4, 8, 16, 32\}$  mT/m respectively.

Both experiments were repeated without external vibrations to measure  $\varphi_G(0)$ . Acquisition time (TA) for all encoding directions for the measurement with one MEG amplitude is 42 s (volunteer 1) and 51 s (volunteer 2), in addition the acquisition of the respective offset phase takes 5.25 s (volunteer 1) and 6.33 s (volunteer 2).

### 3.3 MRE data processing

#### 3.3.1 Wave images

Single encoding-phase contrast wave images were computed for each MEG using Equation (2) (assuming no noise). Dual encoding wave images were computed using combinations of those single encoding images using standard and optimal methods. In addition, OMME was used to combine wave images acquired with different MEGs. The specific MEGs are indicated in each figure in the results section. Wrapped single motion encoding phase images were unwrapped using Laplacian and Flynn based unwrapping algorithm as outlined in the introduction.

#### 3.3.2 Shear wave speed reconstruction

Finally, wrap-free phase images from single and multiple encoding methods were used for reconstruction of SWS maps based on phase-gradient wavenumber recovery to avoid noise amplification by the Laplacian operator which is inevitable in direct inversion techniques [9, 16]. SWS is related to tissue stiffness and will be termed as such in the following. The principle of wavenumber (k-) based multi-component, elasto-visco (k-MDEV) inversion was originally introduced for liver MRE and is outlined in [27]. Since k-MDEV inversion was never applied to brain MRE data before we adapted the spatial filters to the resolution of brain MRE. Compared to k-MDEV proposed for abdominal organs [27], we replaced the linear radial filter in the spatial frequency domain by a radial bandpass Butterworth filter of third order with highpass threshold of 15 1/m and lowpass threshold of 250 1/m.

#### 3.3.3 Noise analysis

Signal intensity and MNR of the wrap-free phase images are important parameters for the subsequent post-processing and final SWS reconstruction. According to our theory, OMME promises wrap-free phase images with MNR corresponding to the highest MEG used for OMME phase recovery. To calculate MNR for experimental data we used the blind noise estimation method of Donoho et al. [6] as outlined and previously applied to MRE data in [3]. Noise estimation in the wavelet domain is expected to be well suited for wave images [1, 22]. We estimated MNR from the dual-tree wavelet transformation of the displacement images with the median absolute deviation of the finest band of wavelet coefficients [6]. The estimated signal power is derived from the L2-norm. Signal and noise levels are estimated from a magnitude threshold based region of the wavefield (see Figure 3i and Figure 8) for all slices and components and averaged afterwards.

## 4 Results

### 4.1 Experimental phantom

Figure 3 presents the waves for the single encoding cases, optimal and standard dual encoding, and OMME using three MEGs. Results are as expected, i.e. both dual encoding methods show the wraps of the low MEG image. The standard and dual encoding methods behave similarly, since  $\beta = 1/2$  and the noise level of the images is low  $\sigma_\varphi \approx 0.02$ , which is estimated from MEG=0 images. The tri-MEG image shows also the dynamic range of the largest MEG. All dual and tri MEG including MEG=8 are fully unwrapped. Figure 4 presents the same waves but colored in a

tighter motion range, in order to put in evidence the gain in the MNR when increasing the number of gradients within OMME in the regions with low motion amplitude, i.e. far from the vibration probe (left part of the pictures).

Figure 5 presents, SWS maps obtained by single and optimal multiple encoding reconstructions compared with Laplace and Flynn unwrapping applied to the single encoding images. In all cases, the SWS maps are more homogeneous towards the center of the phantom and noisier far from the probe, as expected since the wave is damped with decreasing the MNR. However, it is also clear that increasing the MEG reduces the noise in the SWS maps in all cases. Both conventional phase unwrapping algorithms exhibit different drawbacks. Laplacian based unwrapping smooths image details as it can be seen from the disappeared air inclusions in the reconstructed SWS map for the phantom data. The inclusions also disappear with Flynn since it cannot solve correctly the phase jump at the air-heparin boundary.

This artifact increases when the MEG increases, probably because more wraps appear in the wave image amplifying the smoothing effects of the unwrapping algorithm. Flynn becomes more unstable the more wraps occur. In contrast, OMME allows recovering image details, without wraps resulting in smoother SWS maps. A homogeneous appearance of SWS is expected for our homogeneous phantom.

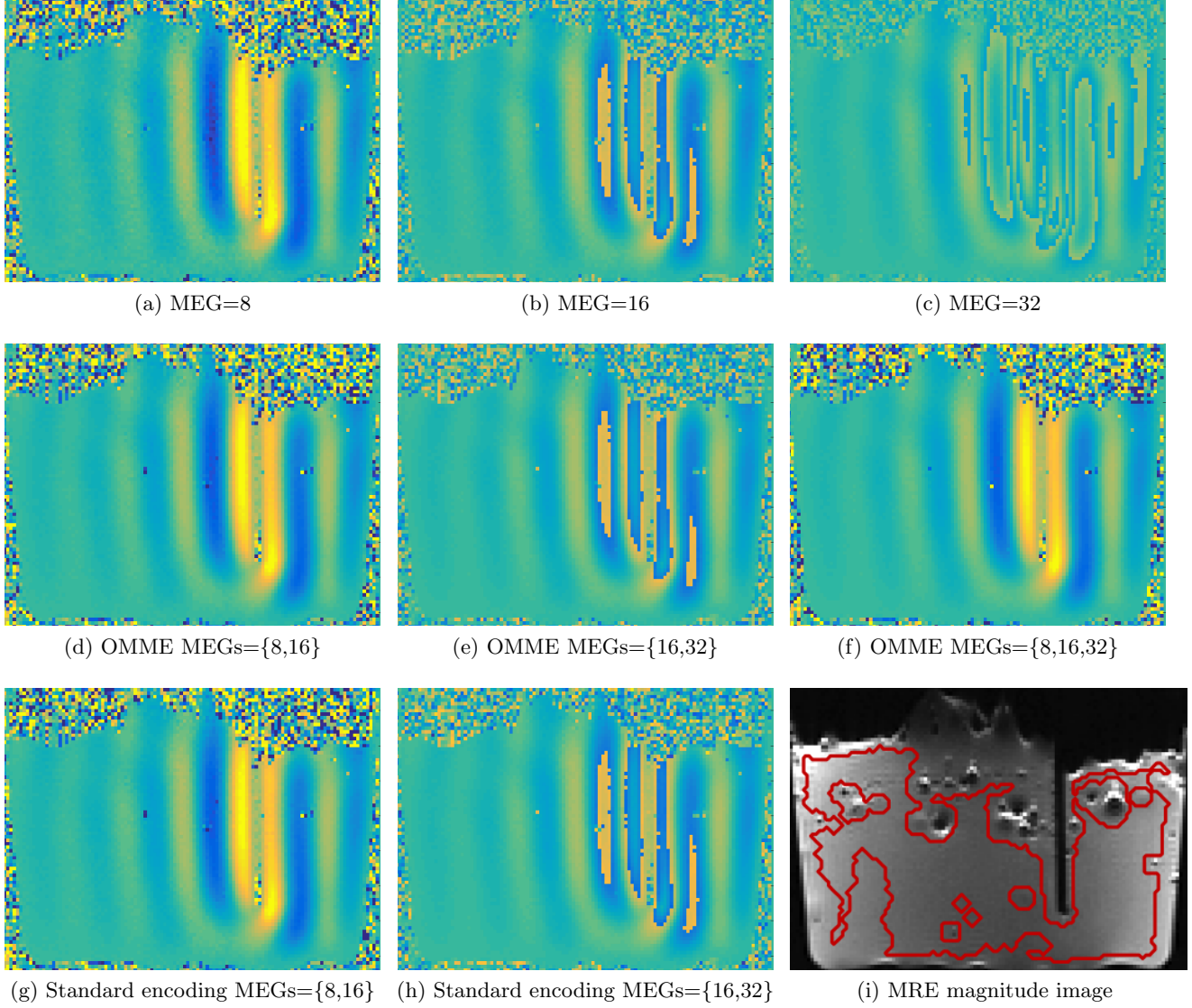


Figure 3: Multiple motion encoding reconstruction in the phantom. Color scale is set in the interval  $\pm 80\%$  of the dynamic range of the MEG=8 image. Large positive values are colored in yellow and negative values in blue, while green being zero. The last image shows the T2 weighted MRE magnitude as geometric reference.

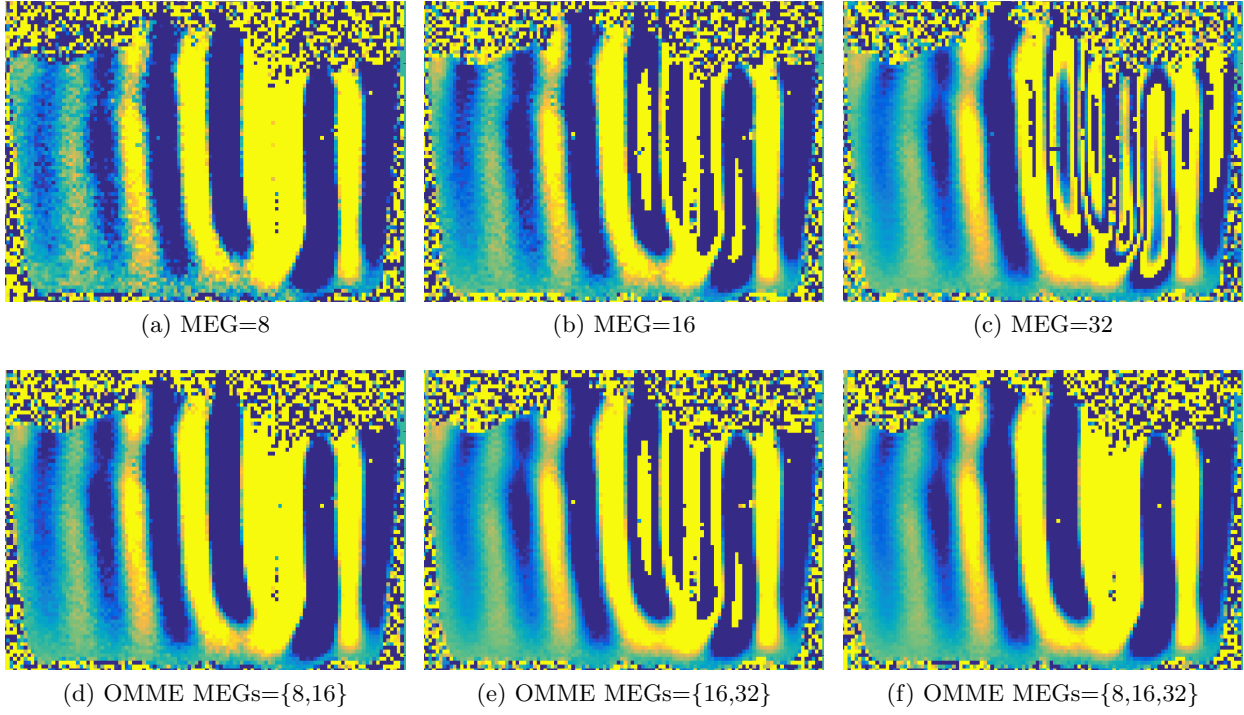


Figure 4: Multiple motion encoding reconstruction in the phantom. Colour scale is set in the interval  $\pm 30\%$  the dynamic range of the MEG=32 image. Large positive values are colored in yellow and negative values in blue, while green being zero.

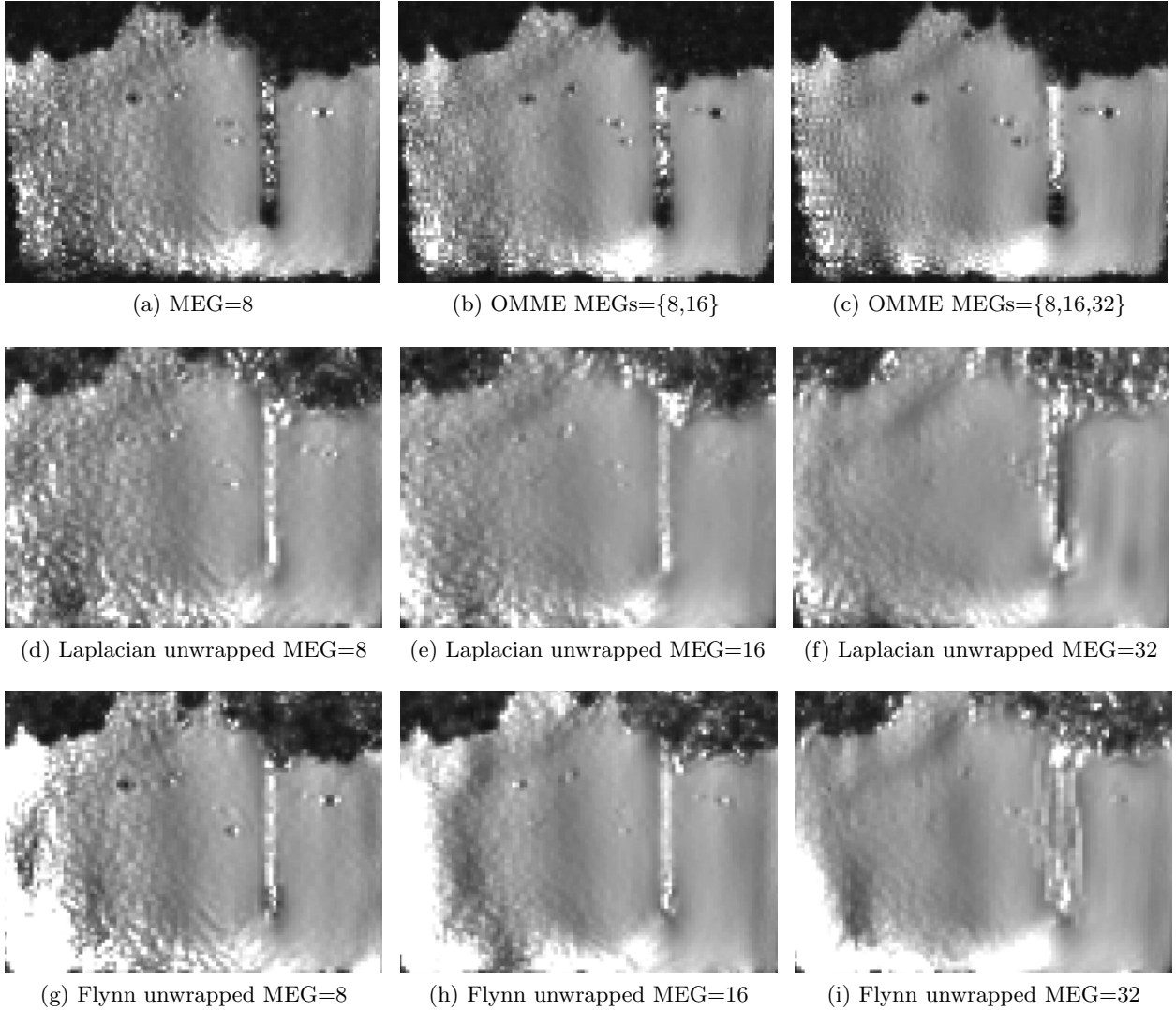


Figure 5: SWS maps reconstructed from k-MDEV at 30.03 Hz vibration frequency for a selected slice in the phantom. The excitation plate is visible on the right side. First row shows OMME results with one (a) to four (d) MEGs combined. The second row shows SWS recovered from Laplacian based unwrapped phase images with MEG of different strength. Last row shows SWS recovered from Flynn unwrapped phase images. Colorbar for SWS maps range from 0 to 1 m/s.

## 4.2 Volunteers

In Figure 6 and 7, we present the wavefields and reconstructed SWS maps for the in vivo brain experiment from volunteer 1, respectively. In this case, we combined four MEGs with OMME to omit standard unwrapping procedures. Compared are SWS reconstructions based on wrap-free phase images from OMME, Laplacian based unwrapping and Flynn unwrapping.

It is well visible that OMME preserves detail in the resulting SWS map which appears more smoothed after applying Laplace and Flynn unwrapping. Especially tissue/air interfaces are sharper



(red arrow) and noise outside the brain is largely reduced. Overall, the contrast of the image is better with OMME.

This example illustrates the capability of OMME to compensate for wraps and noise simultaneously.

We noticed wraps in Figure 6a in the lower part, which the standard dual MEG method cannot unwrap it (see Figure 6e). However, this artifact disappears when combining MEGs 4 and 8 with OMME, and successively including higher MEGs 6f. This is most likely due to the fact that the dynamic range in the MEG 4 image is very close to the actual motion in that region, and hence wraps appear due to the noise.

The checkerboard-like artifacts in the SWS map (red arrow) are resulted by directional filtering in the preprocessing step. This artefact is more noticeable in the volunteer 1 data than in the phantom (Figures 7a-7d), most likely due to the lower SNR in the brain compared to the phantom data. Stronger smoothing could remove the artifact but would also lead to further blurring of the images.

Finally, Figures 8 and 9 show SWS maps for volunteers 1 and 2, respectively, reconstructed from OMME phase images using four MEGs, and Laplacian based unwrapping as well as Flynn unwrapping with the strongest MEG. Additionally, T2 weighted MRE magnitude images are shown for anatomical reference. Red arrows indicate areas where OMME based reconstruction shows higher level of details than unwrapping procedures by fully recovering fluid/tissue boundaries between brain tissue and either ventricles or gyri. The transition between the skull and the brain tissue is also properly reconstructed, while the unwrapping methods smooth that region leading to spurious stiffness values.

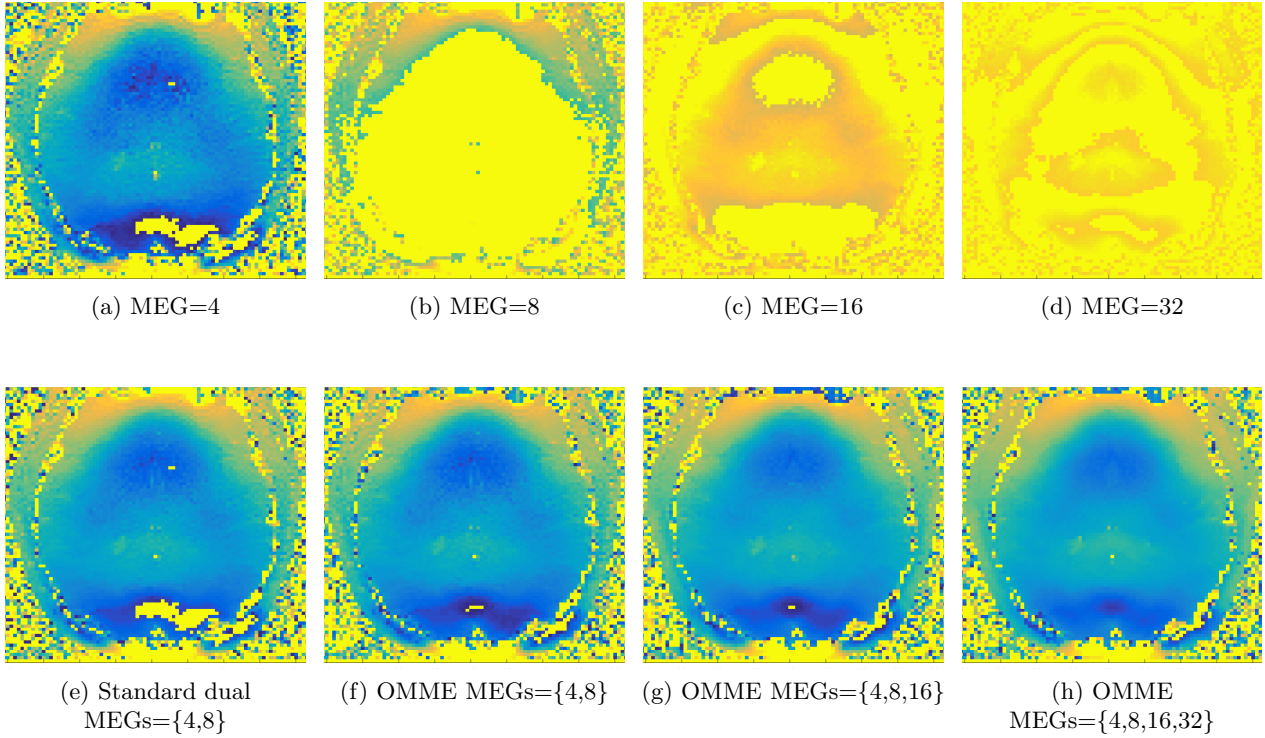


Figure 6: Estimated motion in Volunteer 1, direction of maximal amplitude. Color scale is set in the interval between zero (bright yellow) and minus the dynamic range of the image with MEG=4 image (dark blue) since the wave has mainly positive displacement values. First wraps therefore appear in yellow, nested wraps in orange. The first row shows phase images for a MEG acquisition with increasing MEG amplitude. The second row shows standard dual encoding and OMME combined phase images with increasing amount of MEGs.

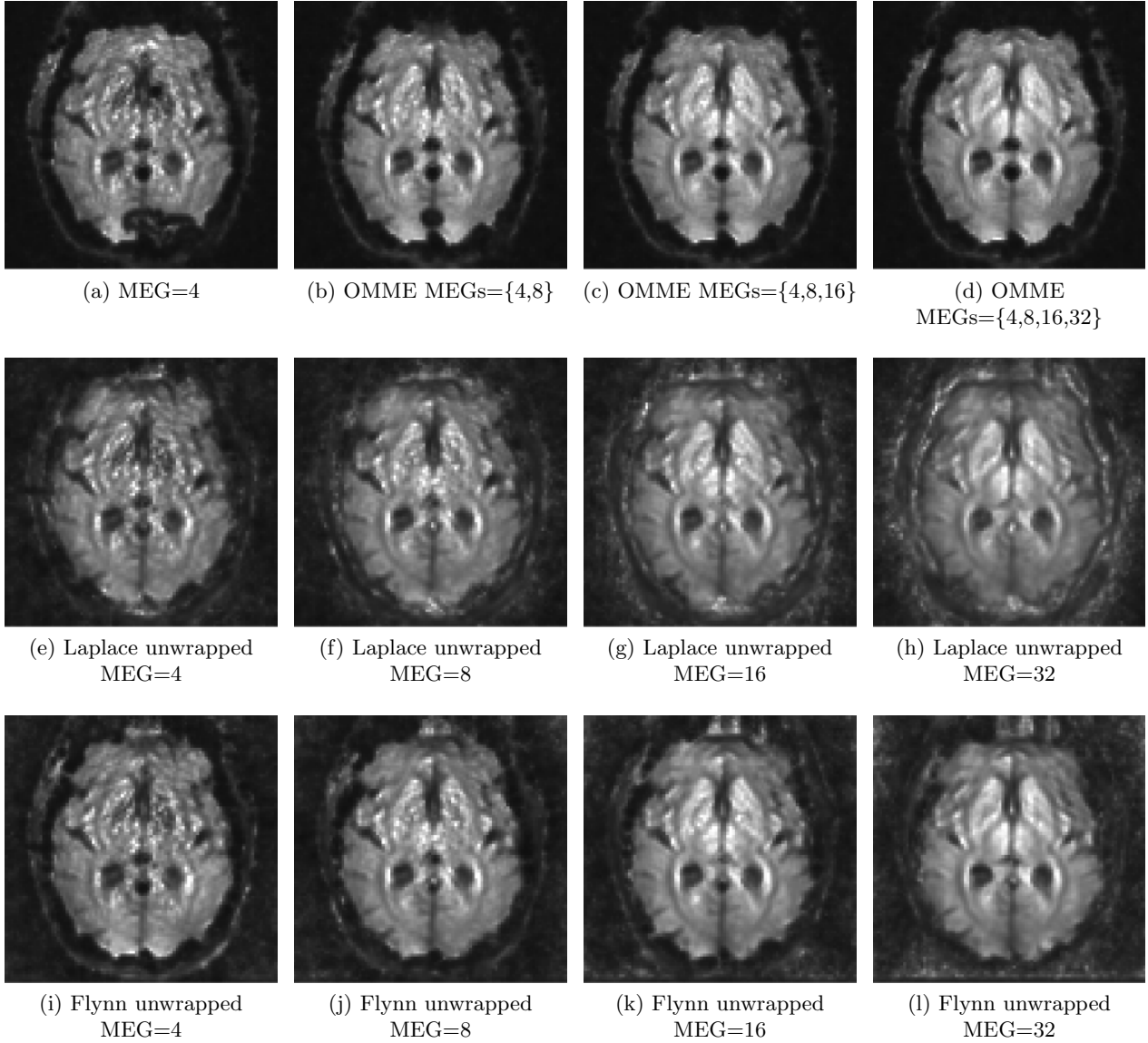


Figure 7: SWS maps for in vivo brain experiment at 25 Hz vibration frequency for a selected slice. First row shows OMME results with one (a) to four (d) MEGs combined. The second row shows SWS recovered from Laplacian based unwrapped phase images with MEG of different strength. Last row shows SWS recovered from Flynn unwrapped phase images. Colorbar for SWS maps range from 0 to 2 m/s.

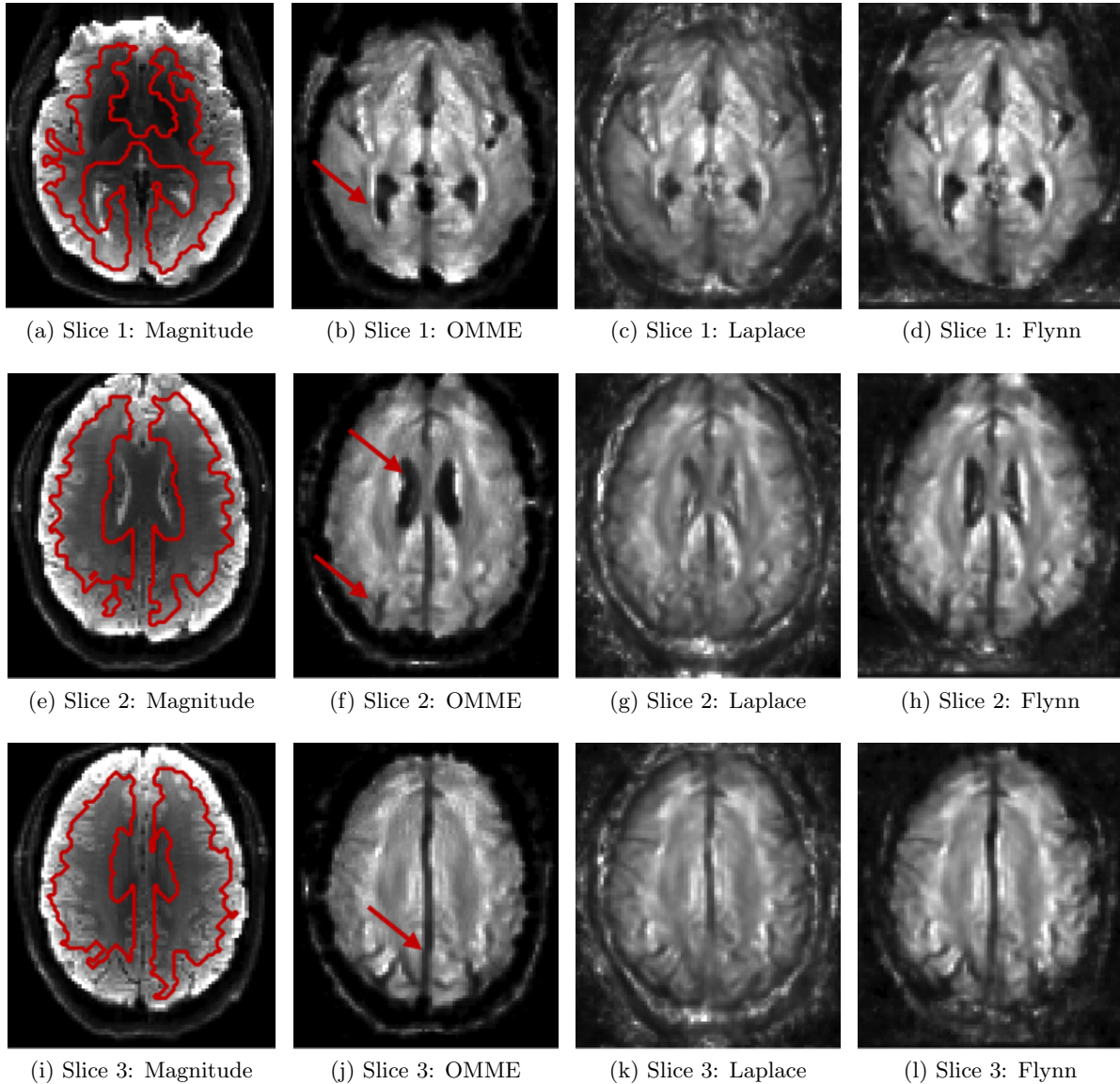


Figure 8: SWS maps for OMME (MEGs={4,8,16,32}) and Laplace and Flynn unwrapping (MEG=32) for **Volunteer 1** at three slices. The anatomical reference image from T2 weighted MRE magnitude is included (red contour use later for noise estimation). Red arrows indicate areas where OMME shows greater contrast in the SWS map. Colorbar for SWS maps range from 0.3 to 1.8 m/s.

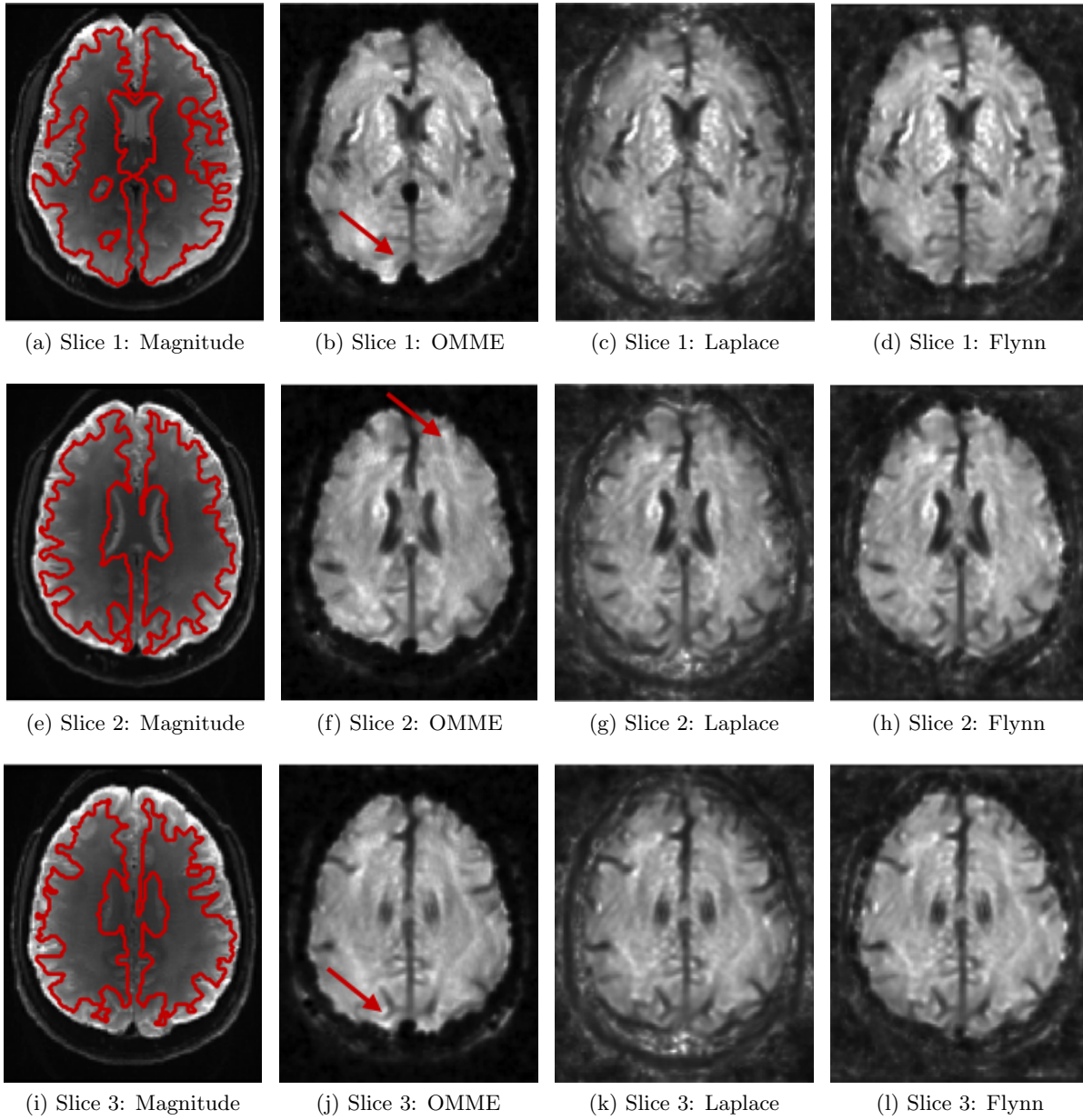


Figure 9: SWS maps for OMME (MEGs={4,8,16,32}) and Laplace and Flynn unwrapping (MEG=32) for **Volunteer 2** at three slices. The anatomical reference image from T2 weighted MRE magnitude is included (red contour use later for noise estimation). Red arrows indicate areas where OMME shows greater contrast in the SWS map. Colorbar for SWS maps range from 0.2 to 2.2 m/s.

### 4.3 Noise analysis

Figure 10 shows the results of the noise analysis for the phantom and in vivo data for the wrap-free phase images recovered from Laplacian and Flynn phase unwrapping and OMME based unwrapping. MNR and signal power are much higher in volunteer 1 than volunteer 2. Overall MNR increases with increasing MEG as signal power stays fairly constant and noise levels decrease as predicted by theory. OMME based unwrapping clearly outperforms the other methods in terms of MNR, since signal power is the highest. Since the underlying displacement is the same for all MEG strengths, the signal power should be constant. Slight decrease in signal power could result from the smoothing effects of the unwrapping procedures.

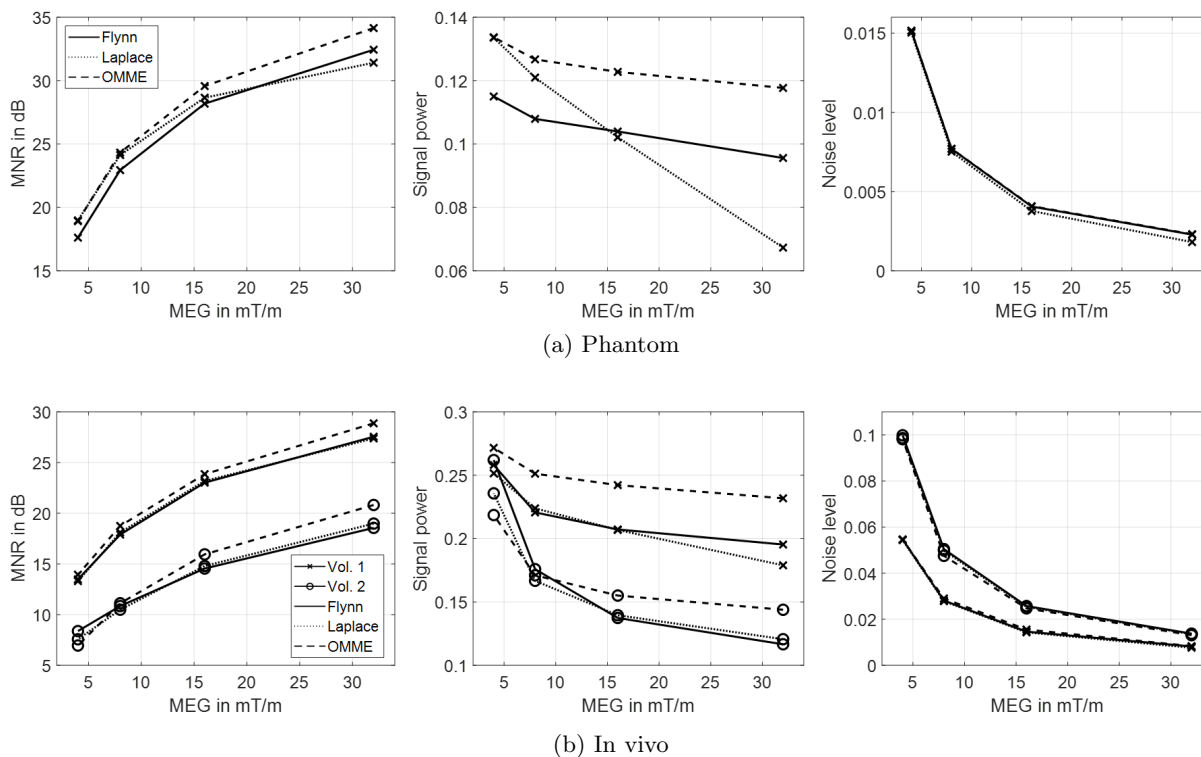


Figure 10: MNR (left), signal power (center) and noise (right) levels estimated from wavelet decomposition for all MEG strengths with Flynn and Laplacian unwrapping and OMME for (a) phantom data and (b) in vivo data. Signal and noise levels were averaged over all slices and components. For OMME, the data points indicate highest MEG used, i.e. at MEG 8, OMME used MEG 8 and 4; at MEG 16, OMME used MEG 16, 8 and 4; at MEG 32, OMME used MEG 32, 16, 8 and 4.

## 5 Discussion

We have developed, theoretically analyzed and assessed in numerical, phantom and volunteer data a new method for combining an arbitrary number of motion-encoded PC-MRI images. The novel method, Optimal Multiple Motion Encoding method (OMME), was analyzed and demonstrated based on MRE measurements, but can be applied to other PC-MRI modalities as well. Dual

encoding was originally developed for flow MRI[4]. To the best of the authors’ knowledge, this is the first reported method to combine an arbitrary number of motion encoded images obtained from different MEGs.

For a fixed effective dynamic range of the imaged motion, OMME presents a superior performance with respect to noise compared to standard dual encoding unwrapping. This was assessed analytically and confirmed numerically in a ”single voxel” experiment. The noise analysis for the experimental data confirm these findings.

It was shown that suppression of noise perturbations is most efficient when  $N$  images are combined which were measured in the dynamic ranges  $d_1, \dots, d_N$  such that  $d_i = 2^{-i+1}d_1$ . This allows the scanner operator to select the largest MEG and the number of measurements  $N$  only, as it is usually done when the MEG is kept fixed.

The OMME was compared against standard unwrapping methods (Laplacian and Flynn). Remarkably, OMME allows to improve the SWS maps by reducing the noise in the wave images without spatial smoothing as Laplace unwrapping does and without unwrapping failure as it may occur with Flynn unwrapping predominantly at boundaries. This showed, in both phantom and volunteer data, that details can be preserved which are otherwise smoothed (out) by standard unwrapping methods. This can be relevant for higher resolution MRE in a variety of applications including tumor detection or characterization of lesion in multiple sclerosis (MS) [25]. Moreover, we showed that standard unwrapping methods smear boundaries between fluid filled spaces and brain tissue. This not only affects the outer boundaries of the brain but also interfaces between tissue and fluid filled ventricles. If tissue mechanical properties are altered at those boundaries, e.g. as a result of impaired CSF-brain barriers in MS [26] OMME based wrap-free MRE phase images could be sensitive to those alterations. Also other interfaces between tumor and healthy tissue could potentially be better resolved. Further, the increased dynamic range of OMME with good MNR properties could be utilized when high frequency vibrations induce heavy wraps near the source and are quickly damped towards small deflection amplitudes inside the tissue under investigation. The potential of OMME for higher frequency MRE needs to be further investigated.

Interestingly, the advantage of the unwrapping robustness of OMME is reduced when the dynamic range increases (less phase-wraps) and MNR decreases. Without heavy wraps, Laplacian and Flynn unwrapping methods perform similar. This means OMME appears to be very suitable for high MNR applications.

As a limitation of OMME, examination times are increased by additional measurements for multiple MEGs. Each additional MEG increases total scan time by the total TA of one measurement. Moreover, the reference phase (i.e. MEGs on and vibration off) needs to be measured, which however is required at one time step only for all encoding directions, adding another  $1/(\text{number of timesteps}) * \text{TA}$ . However, this time investment pays off when phase wraps can be avoided and maps are generated that are more detailed than standard methods. Even resolving wraps only partly supports unwrapping algorithms and permits higher encoding efficiencies than standard MRE towards measurement of damped waves without corrupting high amplitude regions.

OMME can be also applied to other PC-MRI methods like e.g. flow MRI. In that case the dynamic range will be the *venc* parameter. However, some careful noise analysis may be needed when the then phase that does not depend on the motion is measured only once, as it is the case in 4D Flow, since then the phase differences for each *venc* will be correlated. This might be investigated in a future work.

## 6 Conclusion

In this study, we proposed an optimal multiple motion encoding (OMME) method which is suitable for motion sensitive PC-MRI. A detailed theoretical analysis was provided to derive optimal combinations of motion encoding gradients. We applied novel OMME to MRE measurements in phantoms and in vivo human brain. It was shown that OMME allows to recover more tissue details due to its increased MNR ratio within a high dynamic range leading to SWS maps which preserve important details such as discontinuities in the stiffness. Especially for applications of high resolution MRE wrap-free images with proper MNR – as provided by OMME – are desired.

## Conflict of interest

The authors declare no conflict of interest.

## Acknowledgments

H.H. and I.S. acknowledge the funding from the German Research Foundation (GRK 2260 BIOQIC, SFB1340 Matrix in Vision) and from the European Unions Horizon 2020 Program (ID 668039, EU FORCE Imaging the Force of Cancer). C.B. acknowledges the funding from the European Research Council (ERC) under the European Union’s Horizon 2020 research and innovation programme (grant agreement No 852544 - CardioZoom). A.O. acknowledge the funding of Conicyt Basal Program PFB-03, Fondecyt 1151512 and Fondap CR2-1511009. A.O and S.U. acknowledge funding from ANID Millennium Science Initiative Program – NCN17–129.

## A Effective dynamic range in OMME

Here we prove that the effective dynamic range in OMME, corresponding to the smallest period of the cost function

$$J_N(u) = \sum_{j=1}^N \left( 1 - \cos \left( \frac{\pi}{d_j} (u_j - u) \right) \right),$$

is the least common multiplier of  $2d_1, \dots, 2d_N$ , i.e.  $d_{eff} = d_1 a^{N-1}$ , under the assumption that  $d_j = (a/b)^{j-1} d_1$ , with  $a < b \in \mathbb{N}$ .

We proceed as it is usual for these problems: find the smallest possible value  $T > 0$  such that  $J_N(u) = J_N(u + T)$ , i.e.:

$$\begin{aligned} \sum_{j=1}^N \cos \left( \frac{\pi}{d_j} (u_j - u) \right) &= \sum_{j=1}^N \cos \left( \frac{\pi}{d_j} (u_j - u + T) \right) \\ &= \sum_{j=1}^N \left[ \cos \left( \frac{\pi}{d_j} (-u) \right) \cos \left( \frac{\pi}{d_j} (u_j + T) \right) - \sin \left( \frac{\pi}{d_j} (-u) \right) \sin \left( \frac{\pi}{d_j} (u_j + T) \right) \right] \\ &= \sum_{j=1}^N \left[ \cos \left( \frac{\pi}{d_j} u \right) \cos \left( \frac{\pi}{d_j} (u_j + T) \right) + \sin \left( \frac{\pi}{d_j} u \right) \sin \left( \frac{\pi}{d_j} (u_j + T) \right) \right]. \quad (8) \end{aligned}$$



Due to the fact that

$$\cos\left(\frac{\pi}{d_j}(u_j - u)\right) = \cos\left(\frac{\pi}{d_j}u_j\right)\cos\left(\frac{\pi}{d_j}u\right) + \sin\left(\frac{\pi}{d_j}u_j\right)\sin\left(\frac{\pi}{d_j}u\right),$$

Equation (8) becomes

$$\sum_{j=1}^N \left[ \cos\left(\frac{\pi}{d_j}u\right) \left( \cos\left(\frac{\pi}{d_j}(u_j + T)\right) - \cos\left(\frac{\pi}{d_j}u_j\right) \right) + \sin\left(\frac{\pi}{d_j}u\right) \left( \sin\left(\frac{\pi}{d_j}(u_j + T)\right) - \sin\left(\frac{\pi}{d_j}u_j\right) \right) \right] = 0.$$

Note now that the functions  $\cos(\pi u/d_j)$  and  $\sin(\pi u/d_j)$  are linearly independent in  $\mathbb{R}$  for all values of  $j$ . Indeed, using the change of variable  $x = \pi u/d_1/a^{N-1}$  the problem reduces to show that the following functions are linearly independent:

$$\cos(xb^{j-1}a^{N-j}), \sin(xb^{j-1}a^{N-j}), j = 1, \dots, N,$$

which is true since  $a^{N-1} < a^{N-2}b < \dots < b^{N-1}$ . Therefore, we obtain that the following relations need to be satisfied:

$$\cos\left(\frac{\pi}{d_j}(u_j + T)\right) - \cos\left(\frac{\pi}{d_j}u_j\right) = 0, \quad \sin\left(\frac{\pi}{d_j}(u_j + T)\right) - \sin\left(\frac{\pi}{d_j}u_j\right) = 0$$

or using complex variable

$$\exp i\frac{\pi}{d_j}(u_j + T) = \exp i\frac{\pi}{d_j}u_j.$$

This leads to  $T = \{2k_j d_j\}_{\forall k_j}$ . Since this has to hold for all  $j = 1, \dots, N$  simultaneously, it proves that the smallest period  $T$  is the least common multiplier of  $2d_1, \dots, 2d_N$ . This leads to the period being  $T = 2d_1 a^{N-1}$ .

## References

- [1] Eric Barnhill, Lyam Hollis, Ingolf Sack, Jürgen Braun, Peter R Hoskins, Pankaj Pankaj, Colin Brown, Edwin JR van Beek, and Neil Roberts. Nonlinear multiscale regularisation in mr elastography: Towards fine feature mapping. *Medical image analysis*, 35:133–145, 2017.
- [2] Eric Barnhill, Paul Kennedy, Curtis L Johnson, Marius Mada, and Neil Roberts. Real-time 4d phase unwrapping applied to magnetic resonance elastography. *Magnetic resonance in medicine*, 73(6):2321–2331, 2015.
- [3] Gergely Bertalan, Jing Guo, Heiko Tzschätzsch, Charlotte Klein, Eric Barnhill, Ingolf Sack, and Jürgen Braun. Fast tomoelastography of the mouse brain by multifrequency single-shot mr elastography. *Magnetic resonance in medicine*, 81(4):2676–2687, 2019.
- [4] H. Carrillo, A. Osses, S. Uribe, and C. Bertoglio. Optimal dual-vcnc (odv) unwrapping in phase-contrast mri. *IEEE Transactions on Medical Imaging*, 38:1263–1270, 2019.

- [5] Huiming Dong, Richard D White, and Arunark Kolipaka. Advances and future direction of magnetic resonance elastography. Topics in magnetic resonance imaging: TMRI, 27(5):363, 2018.
- [6] David L Donoho, Iain M Johnstone, Gérard Kerkycharian, and Dominique Picard. Wavelet shrinkage: asymptopia? Journal of the Royal Statistical Society: Series B (Methodological), 57(2):301–337, 1995.
- [7] Thomas J Flynn. Two-dimensional phase unwrapping with minimum weighted discontinuity. JOSA A, 14(10):2692–2701, 1997.
- [8] Daniel Fovargue, David Nordsletten, and Ralph Sinkus. Stiffness reconstruction methods for mr elastography. NMR in Biomedicine, 31(10):e3935, 2018.
- [9] Sebastian Hirsch, Ingolf Sack, and Jurgen Braun. Magnetic resonance elastography: physical background and medical applications. John Wiley & Sons, 2017.
- [10] Curtis L Johnson, Hillary Schwarb, Matthew DJ McGarry, Aaron T Anderson, Graham R Huesmann, Bradley P Sutton, and Neal J Cohen. Viscoelasticity of subcortical gray matter structures. Human brain mapping, 37(12):4221–4233, 2016.
- [11] Dieter Klatt, Uwe Hamhaber, Patrick Asbach, Jürgen Braun, and Ingolf Sack. Noninvasive assessment of the rheological behavior of human organs using multifrequency mr elastography: a study of brain and liver viscoelasticity. Physics in Medicine & Biology, 52(24):7281, 2007.
- [12] Adrian Lee, Bruce Pike, and Norbert Pelc. Three-point phase-contrast velocity measurements with increased velocity-to-noise ratio. Magnetic Resonance in Medicine, 33:122–128, 1995.
- [13] Michael Loecher, Eric Schrauben, Kevin Johnson, and Oliver Wieben. Phase unwrapping in 4d mr flow with a 4d single-step laplacian algorithm. Journal of Magnetic Resonance Imaging, 43(4):833–842, 2016.
- [14] Gavin Low, Scott A Kruse, and David J Lomas. General review of magnetic resonance elastography. World journal of radiology, 8(1):59, 2016.
- [15] Yogesh K Mariappan, Kevin J Glaser, and Richard L Ehman. Magnetic resonance elastography: a review. Clinical anatomy, 23(5):497–511, 2010.
- [16] Joaquin Mura, Felix Schrank, and Ingolf Sack. An analytical solution to the dispersion-by-inversion problem in magnetic resonance elastography. Magnetic Resonance in Medicine, 84(1):61–71, 2020.
- [17] Kay M Pepin, Richard L Ehman, and Kiaran P McGee. Magnetic resonance elastography (mre) in cancer: technique, analysis, and applications. Progress in nuclear magnetic resonance spectroscopy, 90:32–48, 2015.
- [18] Ingolf Sack, Jens Rump, Thomas Elgeti, Abbas Samani, and Jurgen Braun. Mr elastography of the human heart: Noninvasive assessment of myocardial elasticity changes by shear wave amplitude variations. Magnetic Resonance in Medicine, 61(3):668–677, 2008.

- [19] Susanne Schnell, Sameer Ansari, Can Wu, Julio Garcia, Ian Murphy, Ozair Rahman, Amir Rahsepar, Maria Aristova, Jeremy Collins, James Carr, and Michael Markl. Accelerated dual-ventric 4d flow mri for neurovascular applications. Journal of Magnetic Resonance Imaging, 46:102–114, 2017.
- [20] Marvin A Schofield and Yimei Zhu. Fast phase unwrapping algorithm for interferometric applications. Optics letters, 28(14):1194–1196, 2003.
- [21] Felix Schrank, Carsten Warmuth, Heiko Tzschätzsch, Bernhard Kreft, Sebastian Hirsch, Jürgen Braun, Thomas Elgeti, and Ingolf Sack. Cardiac-gated steady-state multifrequency magnetic resonance elastography of the brain: Effect of cerebral arterial pulsation on brain viscoelasticity. Journal of Cerebral Blood Flow & Metabolism, 40(5):991–1001, 2020.
- [22] Ivan W Selesnick, Richard G Baraniuk, and Nick C Kingsbury. The dual-tree complex wavelet transform. IEEE signal processing magazine, 22(6):123–151, 2005.
- [23] Siddharth Singh, Sudhakar K Venkatesh, Zhen Wang, Frank H Miller, Utaroh Motosugi, Russell N Low, Tarek Hassanein, Patrick Asbach, Edmund M Godfrey, Meng Yin, et al. Diagnostic performance of magnetic resonance elastography in staging liver fibrosis: a systematic review and meta-analysis of individual participant data. Clinical Gastroenterology and Hepatology, 13(3):440–451, 2015.
- [24] Monvadi Srichai, Ruth Lim, Samson Wong, and Vivian Lee. Cardiovascular applications of phase-contrast mri. American Journal of Roentgenology, 192(3):662–675, 2009.
- [25] Kaspar-Josche Streitberger, Ingolf Sack, Dagmar Krefting, Caspar Pfüller, Jürgen Braun, Friedemann Paul, and Jens Wuerfel. Brain viscoelasticity alteration in chronic-progressive multiple sclerosis. PloS one, 7(1):e29888, 2012.
- [26] Tsuneyuki Takeoka, Yukito Shinohara, Koichi Furumi, and Kosuke Mori. Impairment of blood-cerebrospinal fluid barrier in multiple sclerosis. Journal of Neurochemistry, 41(4):1102–1108, 1983.
- [27] Heiko Tzschätzsch, Jing Guo, Florian Dittmann, Sebastian Hirsch, Eric Barnhill, Korinna Jöhrens, Jürgen Braun, and Ingolf Sack. Tomoelastography by multifrequency wave number recovery from time-harmonic propagating shear waves. Medical image analysis, 30:1–10, 2016.
- [28] Ziyang Yin, Yi Sui, Joshua D Trzasko, Phillip J Rossman, Armando Manduca, Richard L Ehman, and John Huston III. In vivo characterization of 3d skull and brain motion during dynamic head vibration using magnetic resonance elastography. Magnetic resonance in medicine, 80(6):2573–2585, 2018.